Local Reversible Melting in Semicrystalline Poly (dimethylsiloxane): a High-Field Electron Paramagnetic Resonance Study

Journal:	*Macromolecules*
Manuscript ID	ma-2017-00627z.R2
Manuscript Type:	Article
Date Submitted by the Author:	n/a
Complete List of Authors:	Massa, Carlo; Consiglio Nazionale delle Ricerche Istituto per i Processi Chimico-Fisici Unita Organizzativa di Supporto di Pisa Pizzanelli, Silvia; National Research Council (CNR), Istituto di Chimica dei Composti OrganoMetallici (ICCOM) Bercu, Vasile; University of Bucharest, Pardi, Luca; Consiglio Nazionale delle Ricerche Istituto per i Processi Chimico-Fisici Unita Organizzativa di Supporto di Pisa Leporini, Dino; University of Pisa, Dipartimento di Fisica

Local Reversible Melting in Semicrystalline Poly (dimethylsiloxane): a High-Field Electron Paramagnetic Resonance Study

Carlo Andrea Massa,[†] Silvia Pizzanelli,[‡] Vasile Bercu,[¶] Luca Pardi,[†] and Dino Leporini[*,§,†]

Istituto per i Processi Chimico-Fisici-Consiglio Nazionale delle Ricerche (IPCF-CNR), via G. Moruzzi 1, 56124 Pisa, Italy, Istituto di Chimica dei Composti OrganoMetallici-Consiglio Nazionale delle Ricerche (ICCOM-CNR), via G. Moruzzi 1, 56124 Pisa, Italy, Department of Physics, University of Bucharest, Str. Atomistilor 405, Magurele, Jud. Ilfov, Bucharest RO-077125, Romania, and Dipartimento di Fisica "Enrico Fermi", Università di Pisa, Largo B. Pontecorvo 3, 56127 Pisa, Italy

E-mail: dino.leporini@unipi.it

[*]To whom correspondence should be addressed

[†]Istituto per i Processi Chimico-Fisici-Consiglio Nazionale delle Ricerche (IPCF-CNR), via G. Moruzzi 1, 56124 Pisa, Italy

[‡]Istituto di Chimica dei Composti OrganoMetallici-Consiglio Nazionale delle Ricerche (ICCOM-CNR), via G. Moruzzi 1, 56124 Pisa, Italy

[¶]Department of Physics, University of Bucharest, Str. Atomistilor 405, Magurele, Jud. Ilfov, Bucharest RO-077125, Romania

[§]Dipartimento di Fisica "Enrico Fermi", Università di Pisa, Largo B. Pontecorvo 3, 56127 Pisa, Italy

Abstract

The reorientation of the paramagnetic guest 4-methoxy-TEMPO (spin probe) in the disordered fraction of semicrystalline poly(dimethylsiloxane) (PDMS) is investigated by high-field Electron Paramagnetic Resonance (HF-EPR) at 190 and 285 GHz. The distribution of reorientation times is evidenced by accurate numerical simulations of the HF-EPR lineshapes above 200 K. The distribution exhibits a bimodal structure with: i) a broad component corresponding to spin probes with fast and intermediate mobility located in the disordered fraction *far* from the crystallites, and ii) a narrow component corresponding to spin probes with extremely low mobility trapped *close* to the crystallites in a *glassy* environment persisting up to the PDMS melting. The spin probe undergoes an exchange process between the trapped and the more mobile fractions which is accounted for by an equilibrium reversible process with standard Gibbs free energy of reaction per spin probe mole $\Delta G_r^0 \simeq 4\,(\Delta H_m - T\Delta S_m)$, where ΔS_m is the equilibrium melting entropy per monomer mole following the absorption of the heat ΔH_m. The process is interpreted as signature of *reversible tertiary nucleation*, occurring at the intersection of crystalline surfaces, thus suggesting surface roughness of the crystal-amorphous interface. It becomes thermodynamically favored at temperatures higher than $T \sim 209$ K where the onset of PDMS melting is located according to Differential Scanning Calorimetry.

1 INTRODUCTION

In a semicrystalline polymer (SCP) the macromolecules pack together in ordered regions called crystallites which are separated by disordered non-crystalline regions.[1–3] In the last years it has become clearer that an intermediate interfacial region between crystallites and disordered surroundings must be also considered.[1,3–5] The interfacial region is a disordered constrained environment usually referred to as rigid amorphous fraction (RAF).[4] The rest of the non-crystalline region other than RAF is expected to exhibit properties like the completely amorphous bulk polymers and is usually termed as mobile amorphous fraction (MAF). MAF becomes liquid-like above T_g whereas RAF devitrifies even close to or above the melting temperature T_m.[4,6,7] Besides fundamental aspects, a deeper knowledge of RAF is also urged from an applicative point of view since both the amount and the nature of RAF affect the mechanical properties of SCPs.[1,8] It has been found that the crystal-amorphous interface at a molecular level in polyethylene is unexpectedly disorganized when compared to textbook schematic and the surface roughness of lamellae approximately doubles the interfacial area.[9] The stability of RAF is dependent on the perfection of the crystalline phase. When the crystal is made more perfect, i.e. when the cold crystallization temperature is fairly higher than T_g, RAF devitrifies at high temperature .[10] If the crystal is not perfect, devitrification occurs at a temperature that is well separated from the melting of the crystals .[10] Polymers which show a RAF are often the stiffer chain polymers.[11] Nonetheless, RAF has been observed also in one of the most flexible polymers known: poly(dimethylsiloxane) (PDMS).[12–17] A change in the glass transition dynamics for systems exhibiting preponderant nucleation and high percentage of RAF as been noted in semi-crystalline polylactide/clay nanocomposites.[18] Even if in most cases, a three-phase model consisting of crystalline domains surrounded by RAF dispersed in the MAF provides accurate description of the microstructure of semicrystalline polymers, evidence of a continuous distribution of microscopic mobility in SCPs has been also reported.[19,20] It is worth noting that MAF and RAF have been also observed in PDMS chains adsorbed on metal oxide nanoparticles.[21,22] Bimodal nanoarchitectures have been also

reported both at the solid-polymer melt interfaces in equilibrium when polystyrene brushes were adsorbed on Si substrates,[23] and in supported ultrathin polymer films.[24] Caution must be exercised when comparing the features of amorphous-crystalline interfaces in SCPs with the ones of interfaces between adsorbed amorphous polymers and solid substrates owing to, e.g., different roughness of the two kind of interfaces, different interactions of the crystallites and the solid substrates with the amorphous polymers, and the fact that adsorbed chains never penetrate the substrate, whereas polymer chains traverse disordered and ordered regions in SCPs. Nevertheless, such interfaces constitute a reference for comparison with interfaces in SCPs.

Melting of macroscopic polymeric single crystals at equilibrium has been studied under isobaric conditions.[25] A homopolymer is a one-component system and the phase rule permits in this case equilibrium between melt and crystal only at a fixed equilibrium melting temperature T_m^0. Under equilibrium the heat exchange between melt and crystal is *globally* reversible, the total entropy change vanishes so that

$$\Delta H_m = T_m^0 \Delta S_m \tag{1}$$

where ΔS_m is the melting entropy per monomer mole following the absorption of the heat ΔH_m from the liquid. Differently from equilibrium crystals, flexible macromolecules in semicrystalline homopolymers are *globally* out of equilibrium, recognizable by broad melting ranges and the existence of two phases over a range of temperatures at constant pressure.[4] On heating SCPs, escape from their metastable state may occur by *irreversible* processes,[25] like melting of nonperfect crystallites or increase of order by a removal of inner defects.[26] Nonetheless, even in the absence of global equilibrium, several studies concluded that linear, flexible macromolecules in SCPs exhibit *local* equilibria between the surfaces of the individual polymer crystallites and the surrounding amorphous regions which is obtained by *thermodynamically reversible* structure changes, usually referred to as reversible crys-

tallization and melting.[4,5,27] After the first observation in poly(ethylene terephthalate) by Okazaki and Wunderlich in 1997 via temperature-modulated differential scanning calorimetry,[28] reversible melting has been also oberved in other polymers[4,27,29] and ascribed to the attachment and detachment of segments of partially melted macromolecules which are held at or in the vicinity of the crystal growth face.[4,25] In polyethylene and poly(ethylene oxide) crystallites reversibility has been attributed to surface melting and crystallization due to the ability of the chains in the crystals to carry out a sliding diffusion.[5,30]

In a thermodynamically reversible transformation the entropy production, i.e. the dissipation, is negligible. One way to generate such transformations is to drive the system quite slowly so that it always remains very close to equilibrium. This procedure ensures that entropy production is of second order and thus negligible.[31,32] It is known that thermodynamic reversibility has as microscopic counterparts the two, essentially equivalent,[33,34] properties of microscopic reversibility[33] and detailed balance.[35] Motivated by those remarks we searched signatures of an *equilibrium melting/freezing local process* involving RAF and MAF. Our approach recognizes that, in order to make a clear distinction between those regions, structural studies are little informative owing to the small differences of disordered structures.[36] In contrast, more insight is provided by techniques sensitive to *mobility* variations like NMR,[37,38] dielectric relaxation[39] or measurements of the solubility of a gas (for a review see Ref.[5]). Following the same approach, earlier[40,41] and novel[16,17,42] investigations of SCPs addressed the *rotational mobility* of suitable guest radicals (spin probes) in SCPs. They are carried out by Electron Paramagnetic Resonance (EPR),[43] in particular high-field EPR (HF-EPR),[16,17] and exploit the expertise gained on both ice-water mixtures[44–49] and amorphous polymers.[50–57] One major advantage in using guest molecules to investigate SCPs is their selectivity. In fact, assignment of a relaxation process to the amorphous, crystalline or interfacial regions of SCPs is a delicate matter.[13,38,50,51,58–61] From this respect, one has to notice that the crystallites are very often impermeable even to small molecules which are expelled by the ordered regions during the crystallization.[62–65] The confinement of small

tracer molecules in the disordered fraction offers the possibility of selective studies of such regions in SCPs. A similar selectivity is also achieved by dielectric relaxation in that the chain segments incorporated in the polymer crystalline phase do not give rise to a measurable dielectric relaxation and the overall signal is due to the amorphous fraction.[39] The same has been observed by dielectric spectroscopy in systems based on PDMS adsorbed on silica nanoparticles,[66] where various molecular relaxations were recorded (namely, those of MAF and of RAF at interfaces with nanoparticles) while that of RAF around crystals was not recorded, suggesting the larger degree of constraints on polymer chains in the case of crystals.

In a previous HF-EPR study,[16] we investigated the constrained and heterogeneous dynamics in the MAF and RAF fractions of slowly cooled PDMS. It was concluded that RAF is larger than MAF around T_g and it is a small amount of the total amorphous phase at $T_m - 19$ K. Above that temperature, no RAF was detected. No distinctive spectral features associated to RAF were observed. In the present study, *aiming at revealing signatures of reversible local melting*, we adopt an improved strategy[42] to increase the amount of RAF as well as the coupling between the spin probe and PDMS. As first outcome, we provide evidence of RAF persisting up to T_m. As major result, we find that, where RAF is apparent, the spin probe exhibits a *bimodal* distribution of mobility in semicrystalline PDMS, corresponding to a "trapped" fraction and a more mobile one. The exchange process between the two fractions, most probably corresponding to a *reversible tertiary nucleation*, is accounted for by an equilibrium process with equilibrium constant

$$K_{eq} = e^{-\Delta G_r^0/RT} \tag{2}$$

If the trapped and the more mobile fractions of the spin probe are taken as the "reactant" and the "product", respectively, the standard Gibbs free energy of reaction ΔG_r^0 per spin

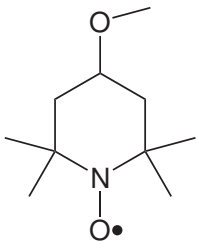

4-methoxy-TEMPO

Figure 1: Chemical structure of the paramagnetic guest (spin probe) mTEMPO (V= 197 Å^3)[67]. The size of the spin probe ($V^{1/3}$ = 0.58 nm) is comparable to the monomer size $v_m^{1/3} = 0.51$ nm and the Kuhn length $\ell_K = 0.50$ nm of PDMS.[68]

probe mole is approximately given by

$$\Delta G_r^0 \simeq 4\,(\Delta H_m - T\Delta S_m) \tag{3}$$

with ΔH_m and ΔS_m introduced in Eq. 1. Eq.3 is interpreted by saying that switching one spin probe from trapped to mobile status involves reversible, equilibrium melting of about four PDMS monomers.

The paper is organized as follows. In Sec.2 experimental details are given. Sec.3 discusses the results. The main conclusions are summarized in Sec.4.

2 EXPERIMENTAL SECTION

2.1 Sample

PDMS and the spin probe 4-methoxy-2,2,6,6-tetramethyl-1-piperidinyloxy (mTEMPO) were purchased from Aldrich and used as received. The weight-average molecular weight M_w of PDMS was 90200 g/mol and polydispersity, M_w/M_n, was 1.96. The molecular size of the spin probe is quite comparable with the one of the PDMS monomer, see Fig.1, and smaller than the RAF thickness, typically a few nanometers.[3] An analysis of the interactions between the radical and PDMS, given in Supporting Information, suggests that the spin probe has good

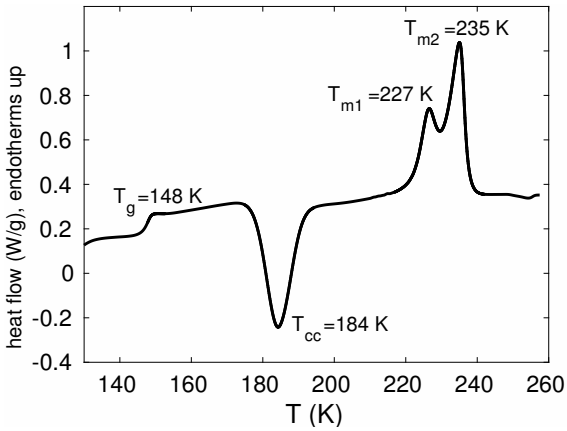

Figure 2: DSC thermogram of the PDMS$_q$ sample.

coupling with PDMS, see also ref.[42] The sample was prepared by dissolving the spin probe and PDMS in chloroform according to the solution method.[69] Then, the solution was heated at about 330 K for 24 h and no residual chloroform was detected by NMR. The spin probe concentration was less than 0.05% in weight. As preliminary characterization, differential scanning calorimetry (DSC) measurements were performed. The procedure was the same as detailed elsewhere,[17] apart from the heating rate which is now 10 K/min. The resulting thermogram, is shown in Fig. 2. It is similar to thermograms obtained for PDMS in similar conditions.[15,25,70] The DSC scan exhibits the following transitions: glass transition (T_g) at 148 K, cold crystallization (T_{cc}) at about 184 K with an exothermic peak characterized by $\Delta \mathrm{H_{cc}} = -26.5$ J/g, and melting onset at about 209 K with two endothermic peaks at 227 and 235 K and $\Delta \mathrm{H_m} = 35.0$ J/g. Henceforth, for simplicity, the melting of the crystallites will be denoted as occurring at about $T_m = 230$ K. By taking $\Delta H_m = 4.619$ kJ/mol,[71] one finds a weight crystallinity fraction of 0.56. The influence of the spin probe has been checked by comparing the DSC thermograms of neat and doped PDMS. We found that the temperatures corresponding to the glass transition and the two endothermic peaks are unchanged within 0.5 K. Instead, doping shifts T_{cc} from 190 K down to 184 K, thus suggesting that the spin probe favors PDMS crystallization.

2.2 Thermal Protocol

The sample (about 0.5 cm^3) was preliminarily *quenched* in liquid nitrogen and put in a Teflon holder. Then, the holder was placed in a single-pass probe cell and finally the whole system was loaded cold into the cooled EPR cryostat. All the HF-EPR data were collected during the subsequent slow heating. The sample was kept about one hour at each temperature before the EPR spectrum acquisition. Quench cooling of PDMS for RAF study was also adopted by Lund et al.[15] The cooling protocol adopted here is different from the one of our previous study of PDMS where the sample was *slowly* cooled below the glass transition.[16,17] Henceforth, we shortly name the PDMS obtained with the two cooling protocols as $PDMS_q$ (quench cooled) and $PDMS_{sc}$ (slowly cooled).

2.3 EPR Measurements and Data Analysis

The EPR experiments were carried out on an ultrawideband EPR spectrometer which is detailed elsewhere.[72] The spectrometer frequencies used were 190 and 285 GHz.

The spin probe has one unpaired electron with spin S=1/2 subject to hyperfine coupling to ^{14}N nucleus with spin I=1. For the calculation of the lineshapes we used numerical routines described elsewhere.[73] The same theoretical approach, i.e. the numerical solution of a Stochastic Liouville Equation, is adopted by alternative computational packages like, e.g., the Matlab-based EasySpin,[74] and the NLSL algorithm.[75] Our in-house software and the other two, given the current available computational power and the simple reorientation model of interest here, are equivalent to evaluate the HF-EPR lineshapes recorded in the present study. The **g** and hyperfine **A** tensor interactions were assumed to have the same principal axes. The x axis is parallel to the N-O bond, the z axis is parallel to the nitrogen and oxygen 2π orbitals, and the y axis is perpendicular to the other two. The principal components of the two tensors (g_{xx}, g_{yy}, g_{zz}, A_{xx}, A_{yy} and A_{zz}) are input parameters to calculate the EPR lineshape. They were carefully measured by simulating the "powder" spectrum, i.e. that recorded at temperature low enough to have a lineshape not influenced

by spin probe reorientation. A_{xx} and A_{yy} values are affected by a large uncertainty because they are small compared to the linewidth. In order to obtain more reliable values, we used the additional constraint $\frac{1}{3}(A_{xx} + A_{yy} + A_{zz}) = A_{iso}$, with A_{iso} being the hyperfine splitting observed in the melt at 255 K and assumed that $A_{xx} = A_{yy}$. The best fit magnetic parameters are $g_{xx} = 2.0096$, $g_{yy} = 2.0058$, $g_{zz} = 2.0017$, $A_{xx} = A_{yy} = 0.62$ mT and $A_{zz} = 3.37$ mT. In all the simulations, the principal components of the tensors were set to these values.

In order to keep the number of adjustable parameters as limited as possible, the spin probe reorientation was modelled as isotropic diffusion, characterized by the rotational reorientation time τ_{SRT}, which is related to the rotational diffusion coefficient D through the equation $\tau_{SRT} = \frac{1}{6D}$. The extension of the model to account for possible anisotropic rotational diffusion of the spin probe was deemed unnecessary.[76] The diffusional model is substantiated by the considerable temperature dependence of the difference between the resonating magnetic fields of the outermost peaks, ΔB, as shown in the Supporting Information. The theoretical lineshape was convoluted with a Gaussian function with a width of 2 G to account for the inhomogeneous broadening. Note that the gaussian convolution affects more the theoretical HF-EPR lineshape close to T_g, e.g. see Fig. S.2 of the Supporting Information, and much less at higher temperatures due to the considerable broadening of the lineshape, e.g. see Fig.4. The spectra expected when a distribution of reorientation times occurs were calculated summing up about 600 spectra characterized by reorientation times in the range 0.01-300 ns, each spectrum being weighted according to the distribution parameters. The best-fit parameters and related uncertainties were obtained by routine procedures.

3 RESULTS and DISCUSSION

3.1 Influence of the thermal protocol on the RAF amount

The thermal protocol outlined in Sec.2.2, involving a first quench-cooling and a subsequent slow heating paused from time to time to collect the HF-EPR data, is expected

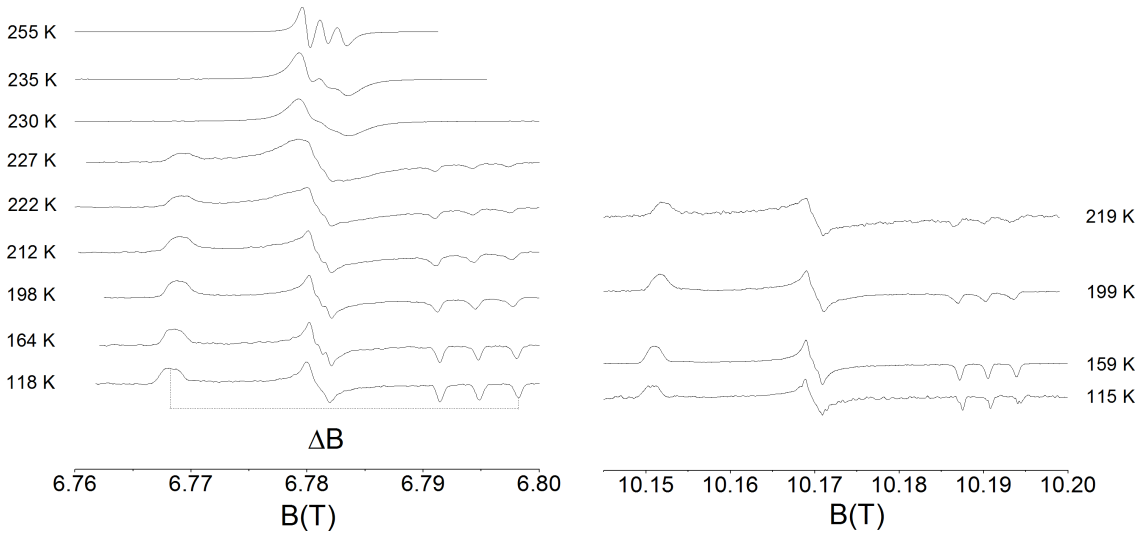

Figure 3: Selected HF-EPR spectra of the spin probe in $PDMS_q$ at different temperatures using the irradiating frequencies of 190 (left hand side) and 285 (right hand side) GHz. ΔB is the difference between the resonating magnetic fields of the outermost peaks observed at lower temperatures.

to yield a larger amount of RAF, as reported, e. g., for poly(oxy-1,4-phenyleneoxy-1,4-phenylenecarbonyl-1,4-phenylene) (PEEK),[25,77] poly(thio-1,4-phenylene) (PPS)[25,78] and poly(butylene terephthalate) (PBT).[79] In fact, in polymers,[80–82] as well as supercooled water,[47–49] quench cooling in the glass region and subsequent re-heating to reach the temperature of interest T ($T_g < T < T_m$) leads to larger polycrystallinity than slow cooling from above T_m down to T. The enhancement is understood in terms of both augmented primary nucleation[25] and increased disorder of the crystallite surfaces. The presence of a large number of small irregular crystallites results in a larger surface area of the crystal phase in comparison to the case of large crystallites with regular surfaces obtained upon slow cooling from the melt. The larger interface between melt and crystallites is anticipated to yield a larger amount of RAF, since the RAF thickness is weakly dependent on both the temperature and the crystallinity[1] and nanometric in size[3] . As to the RAF thickness, e.g., in semicrystalline poly(trimethylene terephthalate), poly(ethylene terephthalate) and poly(phenylenesulfide) one finds 1.1 to 1.6 nm,[83] 2-4 nm[84] and 4 ± 1 nm,[85] respectively. The RAF thickness of PDMS at the interfaces with nanoparticles was found to be 2-3 nm.[86,87] In that case RAF

follows from the formation of strong hydrogen bonding between the oxygens in the PDMS backbone and the surface hydroxyls on the surfaces of silica nanofillers.[86,87] We are not aware of experiments measuring the RAF thickness in semicrystalline PDMS. However, following Ref.[87] and considering the cooperativity length ξ as lower bound, we estimate that the RAF thickness is not thinner than $\xi_{PDMS} = 1.4$ nm.[88]

3.2 HF-EPR Spectra and Dynamic Models

Fig. 3 shows selected first-derivative EPR lineshapes of the spin probe in $PDMS_q$ recorded with the irradiating frequencies of 190 and 285 GHz in the temperature range 115-255 K. The lineshapes of the spectra recorded at the lowest temperatures are those expected for a "powder" sample, independent of the rotational dynamics. At higher temperatures the difference, ΔB, between the resonating magnetic field of the most distant peaks decreases and the sharper details of the lineshape round off, until the features reminding those of the "powder" sample are suddenly lost around $T_m = 230$ K. At T_m, the motional narrowing of the EPR lineshape becomes strong and a triplet structure starts appearing, which is more and more sharpening upon heating. All in all, the changes of the EPR lineshape by increasing the temperature suggest faster and faster reorientation of the spin probe, with abrupt increase of mobility around T_m.

A thorough numerical analysis of the HF-EPR lineshape has been performed and detailed in the Supporting Information. The main results are summarized in the following. Below 200 K a simple model, referred to as single reorientation time (SRT) model, adopting a *single* average reorientation time τ_{SRT}, satisfactorily predicts the lineshape. Differently, in the temperature range between 200 and 227 K the SRT model becomes inadequate, and it is necessary to adopt a different model accounting for a *heterogeneous* rotational dynamics arising from the distribution of environments of the disordered PDMS hosting the spin probe. The heterogeneity is accounted for by a distribution of reorientation times $\rho(\tau)$. In the new

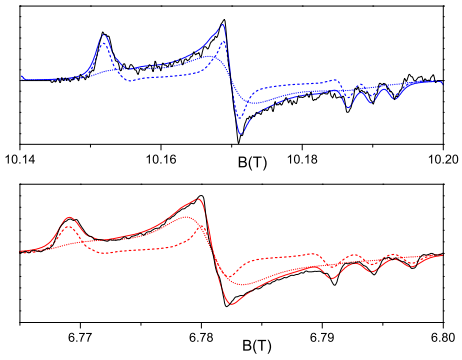

Figure 4: Experimental HF-EPR lineshapes at 190 GHz (bottom) and 285 GHz (top) of the spin probe in $PDMS_q$ at 222 and 219 K, respectively (black lines) compared to the best fits provided by Eq.4 according to the PDT model, Eq.6 (continuous red and blue lines for 190 and 285 GHz, respectively). The contributions due to the PD (untrapped spin probes) and δ (trapped spin probes) components of ρ_{PDT} are superimposed as short-dotted and short-dashed lines, respectively. The best–fit parameters at 190 GHz (285 GHz) are $\tau_{PD} = 0.33$ (0.29) ns, $x = 0.9$ (1.2), $\tau_{trapped} = 21$ (20) ns, $w_{PD} = 0.62$ (0.5).

model the lineshape $L(B)$ is a weighted superposition of contributions

$$L(B) = \int_0^\infty L(B,\tau) \cdot \rho(\tau)\ d\tau \tag{4}$$

where $L(B,\tau)$ is the EPR lineshape corresponding to reorientation time τ. Eq.4 assumes that the PDMS rearrangements are considerably slower than the EPR observation time, about 100 ns. In the presence of dynamical heterogeneity a proper account of the reorientation of the spin probe is provided by the average reorientation time $\langle\tau\rangle$:

$$\langle\tau\rangle = \int_0^\infty \tau \cdot \rho(\tau)\ d\tau \tag{5}$$

The analysis of the HF-EPR lineshape, presented in the Supporting Information, gives clear indications that the distribution of the rotational mobility of the spin probes, $\rho(\tau)$, has bi-modal structure with: i) a broad component corresponding to spin probes with fast and intermediate mobility, and ii) a narrow component corresponding to spin probes with extremely low mobility. The two fractions of the spin probes are expected to be located in

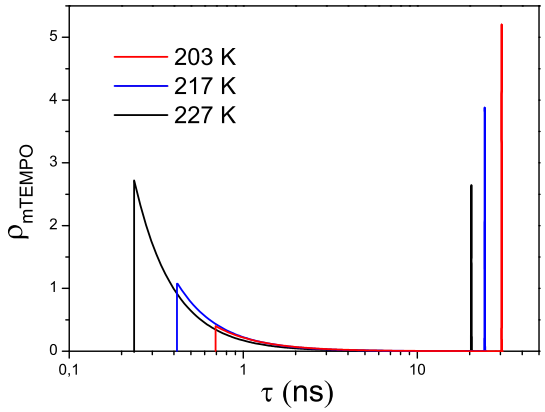

Figure 5: Distribution of the reorientation times of the spin probe in the PDMS$_q$ melting region according to $\rho_{PDT}(\tau)$, Eq. 6. The plots are based on the best-fit parameters listed in Table 1. The broad component at short τ values is $\rho_{PD}(\tau)$, Eq.7, whereas the peak located on the right side of ρ_{PD} corresponds to the δ component accounting for the trapped spin probes.

the disordered fraction *far from* the crystallites, and *trapped close to* the crystallites, respectively. More explicitly, the form of the distribution $\rho(\tau)$ which we adopted, to be denoted as $\rho_{PDT}(\tau)$, is given by:

$$\rho_{PDT}(\tau) = w_{PD} \cdot \rho_{PD}(\tau) + (1 - w_{PD}) \cdot \delta(\tau - \tau_{trapped}) \tag{6}$$

where the broad distribution, $\rho_{PD}(\tau)$, and the narrow one, expressed by the Dirac delta $\delta(\tau - \tau_{trapped})$, refer to the untrapped and the trapped fractions of the spin probe in PDMS$_q$, respectively, and w_{PD} is a weighting factor. We resigned to broaden the Dirac delta since it does not improve significantly the quality of the fit even with one more adjustable parameter. The component $\rho_{PD}(\tau)$ is taken as a power-law distribution (PD) described by the following equation:

$$\rho_{PD}(\tau) = \begin{cases} 0 & \text{if } \tau < \tau_{PD} \\ x \cdot \tau_{PD}^{x} \cdot \tau^{-(x+1)} & \text{if } \tau \geq \tau_{PD} \end{cases} \tag{7}$$

where τ_{PD} is the shortest reorientation time and x is related to the distribution width. Eq.7 follows by a scenario where the reorientation of the spin probe is pictured as a sequence of

Table 1: Best-fit parameters of the heterogeneous reorientation PDT model, Eq. 6, between the onset of melting and T_m+20 K for the spin probe in $PDMS_q$. Homogeneous reorientation accounted for by the single reorientation time τ_{SRT} occurs for $T \geq T_m$. All data are taken from HF-EPR at 190 GHz.

T(K)	x	τ_{PD}(ns)	$\tau_{trapped}$(ns)	w_{PD}	τ_{SRT}(ns)
203	0.67	0.70	30	0.41	
208	0.78	0.65	28	0.47	
212	0.70	0.50	26	0.51	
217	0.81	0.42	24	0.56	
222	0.90	0.33	21	0.62	
227	0.92	0.23	20	0.70	
230					0.18
250					0.075

activated steps over energy barriers with exponential distribution of their heights.[55] In our previous HF-EPR work on semicrystalline $PDMS_{sc}$ we evidenced that the TEMPO spin probe exhibits only a broad distribution of reorientation times with *no* trapped fraction, corresponding to $w_{PD} = 1$ in Eq.6, and that the shape of the broad distribution is better accounted for by the PD distribution, Eq.7, than the log-Gauss distribution.[16] The similarity of the spin probe used in the present study with TEMPO motivated us to describe the broad distribution of the reorientation times with the same form adopted in ref.[16] .

Figure 4 shows an illustrative example of the excellent fitting quality provided by the PDT model. Table 1 lists the best-fit parameters of the PDT model of the spin probe in $PDMS_q$.

Fig.5 shows some representative plots of the distribution $\rho_{PDT}(\tau)$ of the spin probe. It is seen that: i) the broad (ρ_{PD}) and the narrow (δ) components do *not* overlap, and ii) the broad component accounts for the distribution of the shorter reorientation times. The agreement of the PDT model with the experiment covers the range between 200 K and $T_m = 230$ K. As noticed elsewhere,[16] above T_m the high PDMS fluidity averages the distribution of reorientation times quite effectively and narrows considerably the distribution $\rho(\tau)$ so that the description provided by the SRT model is good enough.

We ascribe the change of the weight parameter w_{PD} in Eq.6 with the temperature to a change of the RAF and MAF environments where the spin probes are located. However, migration of the spin probes between the two disordered regions is, in principle, also possible so that the observed population shift between the broad (ρ_{PD}) and the narrow (δ) components could be interpreted in an alternative way as due a change of the residence time of the spin probe in each of the two environments, even if the latter do *not* change with the temperature. Migration is driven by the diffusivity of the spin probe. We now provide an argument suggesting that the latter is negligible within the typical observation time of EPR $\tau_{obs} \sim 100$ ns. To this aim, we consider the diffusion of the perylene dye PMI in PDMS with $M_w = 63K$ and $M_w/M_n = 1.71$[89] (our PDMS sample has $M_w \sim 90K$ and $M_w/M_n = 1.96$, see Sec.2.1). The hydrodynamic radius of PMI in toluene is $R_{PMI} = 0.53$ nm[89] to be compared with $R_{TEMPONE} = 0.237$ nm in toluene[90] where TEMPONE is a spin probe quite similar to the spin probe used in the present study. We do not expect strong dependence of the hydrodynamic radius of this class of nitroxide spin probes on the host, e.g. TEMPO spin probe, quite similar in shape and size to TEMPONE and our spin probe, exhibits $R_{TEMPO} = 0.26$ nm in the supercooled molecular liquid o-terphenyl.[91] By extrapolating the experimental data, we find that the diffusion coefficient of PMI in the MAF is $D^{MAF}_{PMI} \simeq 4 \cdot 10^{-4}$ nm^2/ns at 200 K, i.e. $T_{cc} + 16$ K[89]. In ref.[89] one finds that the diffusivity of small molecules hosted in PDMS scales approximately as the inverse of the squared hydrodynamic radius. Accordingly, we estimate that the diffusion coefficient of our spin probe mTEMPO in MAF at 200 K is given by $D^{MAF}_{mTEMPO} \simeq D^{MAF}_{PMI} \cdot (R_{PMI}/R_{TEMPONE})^2 \simeq 2 \cdot 10^{-3}$ nm^2/ns, corresponding to a root mean square displacement $(6 D^{MAF}_{mTEMPO}\, \tau_{obs})^{1/2} \simeq 1.1$ nm. The same evaluation at $T_m = 230$ K yields $\simeq 3$ nm. Those displacements must be compared with the typical interlamellar spacing where amorphous PDMS locates. We are not aware of measurements of this spacing in PDMS. It is about 7 nm in poly(ϵ-caprolactone)[92] and increases from ~ 7 to 17 nm with the molecular weight in polyethylene[93] and from 5.9 to 7.2 nm with the temperature in poly(ethylene oxide).[94] Then, during τ_{obs}, the spin probe is

anticipated to wander through MAF to a limited extent. Diffusivity in RAF is much lower. To estimate the drop of the mobility, one notices that the structural relaxation time τ_α in RAF is about three orders of magnitude longer than in MAF.[14,15] Assuming that the same drop occurs for the diffusivity, one concludes that the spin probe displaces in RAF about $\simeq 0.03$ nm at 200 K and about $\simeq 0.08$ nm at T_m. We estimated the RAF width as large as 1.4 nm at least, see Sec.3.1. Then, during τ_{obs}, according to the previous analysis, only a tiny amount of spin probes in RAF escapes to MAF and, conversely, the spin probes leaving MAF penetrate into RAF negligibly. In conclusion, migration of spin probes between RAF and MAF within τ_{obs} is anticipated to be virtually absent and have negligible effects on the HF-EPR lineshape.

3.3 Homogeneous and Heterogeneous Rotational Dynamics of the Spin Probe in PDMS: Evidence of MAF and RAF

We are now in a position to characterize the rotational dynamics of the spin probe in $PDMS_q$. The results are summarized in Fig. 6 and Fig. 7. They exhibit little dependence on the frequency, suggesting that complete information on the distribution of the reorientation times is collected. From the lowest temperatures below T_g, passing through T_{cc}, up to about 200 K, the spin probe exhibits homogeneous dynamics well accounted for by the single reorientation time τ_{SRT} of the SRT model with no need to invoke any distribution of the reorientation times. The temperature dependence of τ_{SRT} is plotted in Fig. 6. The absence of any signature affecting τ_{SRT} at $T_{cc} \sim 184$ K indicates that the HF-EPR signal of the spin probe does not detect the formation of the crystals occurring on heating during data collection. An Arrhenius fit of the τ_{SRT} values in the low temperature range provides an activation energy of 6.2 ± 0.3 kJ/mol. In the range between liquid helium temperature and 130 K incoherent neutron scattering and NMR found a value of 6.4 kJ/mol for the activation energy of methyl jumps about the C_3 axis in PDMS.[95] A somewhat lower value, 4.6 kJ/mol, was determined by quasi-elastic neutron scattering.[96] The comparison with the reported activation energy

of the spin probe suggests good coupling between the spin probe reorientation and local motions around T_g.

As pointed out in Sec.3.2, on approaching the onset of PDMS melting ($\simeq$ 209 K), HF-EPR reveals that the reorientation of the spin probe is heterogeneous, i.e. two fractions of spin probes with distinct rotational mobilities become apparent: i) an untrapped, faster fraction with a power-law distribution of reorientation times and ii) a trapped fraction, being characterized by a single reorientation time $\tau_{trapped}$, e.g. see Fig.5. Fig. 7 (top) shows that, on increasing the temperature, the weight of the untrapped fraction increases. Fig. 6 shows that the Arrhenius temperature dependence of the reorientation time of the trapped fraction $\tau_{trapped}$, observed up to T_m, is in *ideal continuation* of the one of the single reorientation time τ_{SRT} characteristic of the spin probe reorientation below $\sim T_{cc}$.[42] These findings suggest that, on increasing the temperature above 200 K, a part of the spin probes persists in the glassy dynamics up to T_m, whereas an increasing fraction leaves the trapped fraction and accelerates its reorientation in a heterogeneous way with a power-law distribution of correlation times, see Fig. 7 (top). The heterogeneity decreases upon heating, as signaled by the mild increase of the width parameter x in Fig. 7 (bottom).

The presence of a *trapped, glassy fraction* of the spin probe between T_{cc} and T_m is striking evidence that it is located in RAF.[4] On the other hand, arguments will be given below and in Sec.3.4 supporting the conclusion that the faster fraction has to be attributed to spin probes located in MAF and in a region with an intermediate mobility between that of the glassy fraction and of MAF.

The melting of the PDMS crystallites at about T_m is signaled by dramatic changes of the HF-EPR lineshape, see Fig. 3. The numerical analysis reveals that the average reorientation time $\langle\tau\rangle$, defined in Eq.5, drops by almost two orders of magnitude upon heating from 227 K to T_m, see Fig. 6. To better understand the origin of the drop, we carefully scrutinized the distribution of reorientation times ρ_{PDT}, Eq. 6. It was found that the distribution disappears above T_m and both the trapped δ fraction and the one with

the power-law distribution collapse to the same single reorientation time τ_{SRT}, namely the heterogeneous rotational dynamics becomes homogeneous. Quite interestingly, the faster spin probes of the distribution, i.e. the ones with $\tau \sim \tau_{PD}$, do not sense the PDMS melting since the temperature dependence of τ_{PD} observed *below* T_m smoothly joins the reorientation time of the spin probe in the PDMS melt *above* T_m, see Fig. 6. As already noted,[16] this scenario strongly suggests that the faster spin probes are localized in MAF.

Above 230 K the reorientation time of the spin probe in the PDMS melt is thermally activated with an activation energy of 20.9 ± 0.4 kJ/mol. The value is in good agreement with previous estimates concerning several nitroxide spin probes in PDMS melt by X-band EPR (19.2 kJ/mol)[51] and HF-EPR (18.8 kJ/mol)[16] and is comparable to the activation energy of PDMS segmental dynamics (14.6 kJ/mol).[96] The little dependence of the activation energy on the choice of the spin probe suggests that the latter is coupled to the structural relaxation above T_m, as already observed for spin probes dissolved in polymer melts far from T_g,[53] and in particular for PDMS.[16] From this respect, one notices that the reorientation time of the spin probe in PDMS is $\simeq$ 75 ps at 250 K (from HF-EPR at 190 GHz), which is comparable to the estimate of 32 ps[15] from dielectric data on PDMS. To better scrutinize the coupling between the spin probe rorientation and the α relaxation in the PDMS melting region, we compared the rotational dynamics of the spin probe with the segmental relaxation time of PDMS. To this aim, we used the Vogel-Fulcher-Tammann (VFT) law:

$$\tau_{VFT} = \tau_0 \exp\left[\frac{B}{T - T_0}\right] \tag{8}$$

where B and T_0 are parameters associated to PDMS whereas τ_{VFT} and τ_0 are the reorientation times of the spin probe at the finite temperature T and infinite temperature, respectively. To match the reorientation time of the spin probe with the PDMS relaxation time we adjusted τ_0, keeping constant all the other parameters. The results are shown in Fig. 8. Indeed, it is seen good agreement of τ_{VFT} with the reorientation time of the spin probe above T_m.

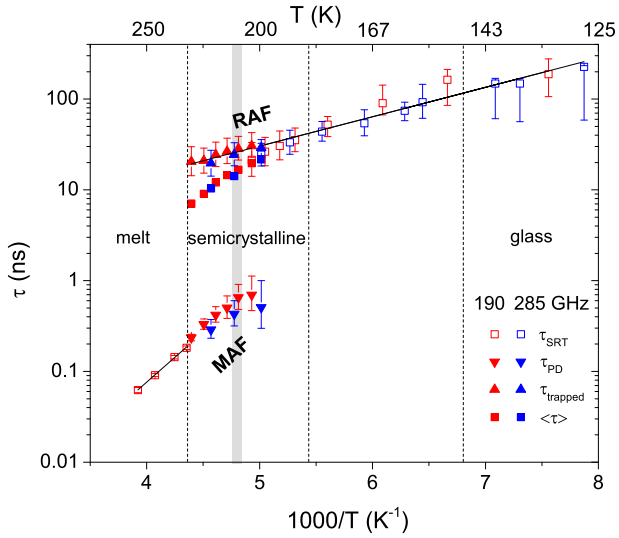

Figure 6: Temperature dependence of the rotational dynamics of the spin probe in PDMS$_q$: characteristic times τ_{SRT}, τ_{PD}, $\tau_{trapped}$ and average reorientation time $\langle\tau\rangle$, see Eq.5 and Eq.6. The dashed vertical lines mark the glass transition at T_g, the cold crystallization at T_{cc}, and the melting transition at T_m, whereas the gray region highlights the range of the onset of PDMS melting ($\simeq$ 209 K) as detected by DSC, see Sec.2.1. The low-temperature and the high-temperature straight lines are Arrhenius fits with activation energies 6.2 $\pm$ 0.3 and 20.9 $\pm$ 0.4 kJ/mol, respectively. Error bars smaller or comparable to the data point symbols are not reported.

Noticeably, below T_m and down to about $T_m - 30$ K, τ_{VFT} agrees with τ_{PD}, the shortest reorientation time of the PDT distribution. The finding that the *faster* spin probes track the segmental motion of PDMS melt also below T_m strikingly confirms our conclusion that they are confined in MAF. This conclusion is also supported by the near proportionality across the PDMS melting region between the reorientation time of the spin probe and the relaxation time of the amorphous phase τ_{AP} measured by dielectric spectroscopy,[15] which we identify with the MAF relaxation time, see Fig. 8.

3.4 Partition of the spin probes in amorphous PDMS above T_g

The present Section discusses the partition of the spin probes in RAF and MAF and proposes a procedure to estimate the RAF amount. It also considers the distribution of the rotational mobility of the spin probes in RAF, which, according to the discussion in Sec.3.2, corresponds

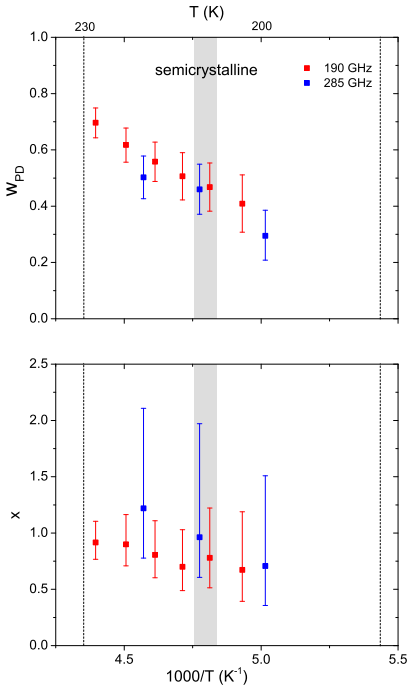

Figure 7: Top: weight of the untrapped fraction of the spin probe, see Eq. 6; bottom: width parameter of the untrapped fraction, see Eq.7 and Eq. 6. The dashed vertical lines mark the cold crystallization at T_{cc}, and the melting transition at T_m, whereas the gray region highlights the range of the onset of PDMS melting ($\simeq$ 209 K) as detected by DSC, see Sec.2.1.

to two subsets pertaining to the trapped and the untrapped spin probes. The former is found to be the most populated.

3.4.1 Homogeneous spatial distribution of the spin probes in amorphous PDMS above T_g

When recording the HF-EPR signal, the spin probe is *homogeneously* distributed in amorphous PDMS above T_g, i.e., the spin probe concentrations in MAF and RAF are equal. To argue the previous statement, we first note that the spin probe is homogeneously dispersed in the PDMS melt *before* quench, as assured by the method of sample preparation, see Sec.2.1. After the quench, and following the nucleation and growth of the crystalline fraction, a part of the spin probes is expelled outside the crystallites. The concentration of the spin probes

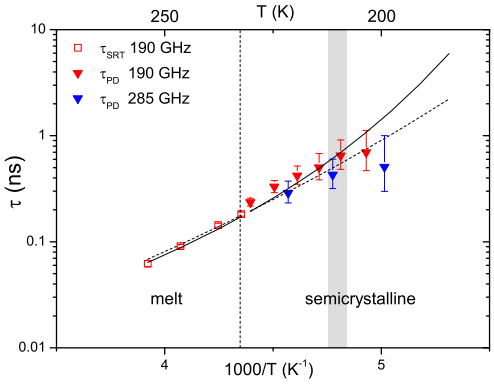

Figure 8: Rotational dynamics of the faster fraction of the spin probes across the melting region of PDMS as accounted for, below 227 K, by the shortest reorientation time of the PDT distribution τ_{PD}, see Eq.7 and Eq. 6. Above 227 K the rotational dynamics is homogeneous with single reorientation time τ_{SRT}. The dashed vertical line marks T_m and the gray region shows the range of the onset of PDMS melting ($\simeq$ 209 K). The dashed line is the best-fit of the data according to the VFT law, Eq. 8. The VFT parameters are set to those of the PDMS melt ($B = c_1^0 \cdot c_2^0 \ln 10 = 971$ K, $T_0 = T_{0_{WLF}} - c_2^0 = 81$ K, where c_1^0, c_2^0 and $T_{0_{WLF}}$ are taken from Ref.[97]). τ_0 was set to the value of 0.00027 ns in order to fit with the data above T_m. The continuous line plots the VFT law, Eq.8, with $\tau_0 = 0.0012$ ns and other parameters as the relaxation time of the amorphous phase τ_{AP} measured by dielectric spectroscopy,[15] i.e. $B = 482$ K and $T_0 = 131$ K.

in amorphous PDMS is initially inhomogeneous with later homogenisation by diffusion. To ensure proper recovery of the homogeneity, after any temperature change, an equilibration time of one hour is warranted before recording the HF-EPR signal, see Sec.2.2. To show the adequacy of the equilibration procedure, we consider the estimate of the diffusion coefficient of the spin probe in RAF and MAF given in Sec.3.2, $D^{RAF}_{mTEMPO} \simeq 10^{-3} D^{MAF}_{mTEMPO}$ with $D^{MAF}_{mTEMPO} \simeq 2 \cdot 10^{-3}$ nm^2/ns at 200 K, i.e. T_{cc} + 16 K. At that temperature, during the equilibration, the spin probe diffuses in the RAF and the MAF over about 6.6 μm and 200 μm, respectively. Those displacements are much larger than the characteristic length scales of semicrystalline polymers. In fact, the spherulites - the spheroidal aggregates of lamellar crystallites spaced by interstitial amorphous regions with size of several nanometers, see Sec.3.2 - have typical size in the range 1-100 μm (see ref.,[98] Table 7.2), whereas the RAF is nanometric in size, see Sec.3.1. Note that, given the small size of the spin probe

(~ 0.58 nm, see Fig.1), the spin probes are expected to be expelled by the crystallites but *not* from the spherulites, i.e. they are dispersed in *all* the amorphous PDMS. The previous analysis provides a sound basis to conclude that the spin probes are *homogeneously* distributed across all the amorphous PDMS above T_g after the preliminary equilibration period before recording the HF-EPR signal.

3.4.2 Estimate of RAF in PDMS

An important consequence of the findings in Sec.3.4.1 is that the relative weights of the spin probes found in RAF and MAF may be interpreted as relative weights of MAF and RAF. We now exploit this feature by presenting a procedure to estimate the RAF amount X^i_{RAF} in PDMS subject to the quench cooling ($i = q$, present work) and to the slow cooling ($i = sc$, Ref.[16]) protocols by using the results concerning the reorientation of the spin probes. The spin probe used in the case of PDMS$_{sc}$ was TEMPO, quite similar to the spin probe of the present study.[16] Due to the presence of the spin probes only in the non-crystalline PDMS, X^i_{RAF} is evaluated with respect to the *non-crystalline* PDMS so that the MAF amount is given by

$$X^i_{MAF} = 1 - X^i_{RAF} \qquad i = q, sc \tag{9}$$

The procedure to estimate the RAF amount was inspired by the finding, shown in Fig.8, that for $T > 200$ K the reorientation time of the fastest fraction of the spin probes, expected to be located in MAF, is well coupled to the MAF relaxation time, very close to the α relaxation time. We estimate X_{RAF} via the relation:

$$X^i_{RAF} = \int_{\tau^*_{RAF}}^{\infty} \rho^i(\tau)\, d\tau \qquad i = q, sc \tag{10}$$

where $\rho^i(\tau)$, Eq.6, is the distribution of the reorientation times of the spin probe in PDMS with i-th thermal history. For $i = q$, the spin probe has $w_{PD} \leq 1$, whereas, for $i = sc$, TEMPO has $w_{PD} = 1$, owing to the absence of the trapped fraction.[16] Eq. 10 assumes that

all the spin probes with reorientation time τ^*_{RAF} or longer are located in RAF. In order to define the maximum rotational mobility of the spin probes in RAF, $1/\tau^*_{RAF}$, we require that the fastest spin probes in RAF are coupled to RAF as the fastest spin probes in MAF are coupled to MAF, i.e.

$$\tau^*_{RAF} = \frac{\tau_{PD}}{\tau_{MAF}} \cdot \tau_{RAF} \tag{11}$$

where τ_{MAF} and τ_{RAF} are the characteristic relaxation times of MAF and RAF, respectively. We consider the data for the spin probe in Table 1 and take τ_{RAF} and τ_{MAF} from the VFT laws of τ_{CAP} and τ_{AP} of Table 1 of ref.[15] , respectively. At 212 K we find $X^q_{RAF} = 0.57$ in $PDMS_q$. The same procedure, when applied to $PDMS_{sc}$ by using the data for TEMPO presented in Ref.,[16] yields $X^{sc}_{RAF} = 0.14$ at the same temperature. The inequality $X^q_{RAF} > X^{sc}_{RAF}$ is consistent with our expectation of larger RAF in $PDMS_q$ than in $PDMS_{sc}$. Notice that in Ref.[16] we identified τ^*_{RAF} with τ_{RAF} and found $X^{sc}_{RAF} = 0.08$ for $PDMS_{sc}$. According to Eq. 11, that identification corresponds to set $\tau_{PD} = \tau_{MAF}$. Instead of the strong assumption that the reorientation times of the faster spin probes in RAF and MAF are *equal* to the ones of the PDMS segments in the corresponding amorphous fractions, Eq.11 adopts the more conservative viewpoint that they are *proportional* to the PDMS relaxation times with equal proportionality constant, as it follows by assuming negligible dependence of the coupling between the spin probe and PDMS on the MAF/RAF character of the non-crystalline fraction.

3.4.3 Mobility distribution in RAF: trapped and untrapped spin probes

The Section 3.4.2 addresses the partition of the spin probes in RAF and MAF depending on their reorientation times, namely spin probes with reorientation time longer than τ^*_{RAF} are in RAF, otherwise in MAF.

It is always found that τ^*_{RAF} is *shorter* than the reorientation time of the trapped fraction of the spin probes $\tau_{trapped}$, i.e. the trapped spin probes, evidenced in Sec.3.2 and dynamically characterized in Sec.3.3, are in RAF. Reminding that $\tau_{trapped}$ is the longest reorientation

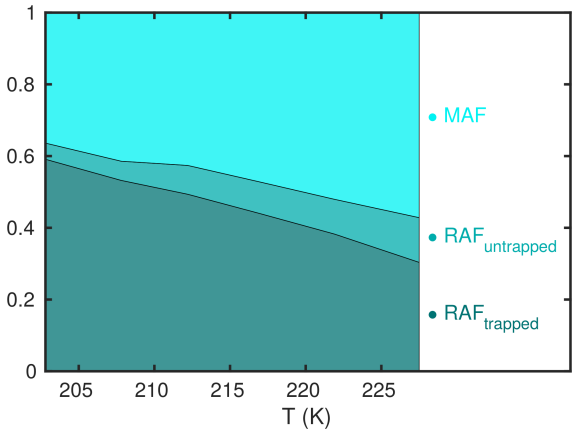

Figure 9: Composition diagram of the non-crystalline part of $PDMS_q$ according to the rotational mobility of the spin probe in the temperature range 203-227 K, as detected by HF-EPR at 190 GHz. The diagram is expressed in terms of X^q_{MAF}, $X^q_{RAF_{trapped}}$ and $X^q_{RAF_{untrapped}}$, as defined by Eq.9, Eq.13 and Eq.14, respectively. On increasing the temperature, the spin probe is increasingly located in MAF and less trapped in RAF.

time of the spin probes, see Fig.5, the rest of the spin probes in RAF, henceforth denoted as "untrapped", has reorientation time in the range $\tau^*_{RAF} \leq \tau \leq \tau_{trapped}$. The previous remarks suggest to split the spin probes in RAF in two subsets pertaining to the trapped and the untrapped spin probes and express the fraction of spin probes in RAF in the quenched sample, X^q_{RAF} as:

$$X^q_{RAF} = X^q_{RAF_{trapped}} + X^q_{RAF_{untrapped}} \tag{12}$$

where replacing Eq.6 in Eq.10 yields:

$$X^q_{RAF_{trapped}} = 1 - w_{PD} \tag{13}$$

$$X^q_{RAF_{untrapped}} = w_{PD} \cdot \int_{\tau^*_{RAF}}^{\tau_{trapped}} \rho^q_{PD}(\tau)\, d\tau \tag{14}$$

It is seen that the trapped fraction of the spin probes in RAF is the largest one. As an example, at 212 K $X^q_{RAF} = 0.57$ with $X^q_{RAF_{trapped}} = 0.49$. We have evaluated $X^q_{RAF_{trapped}}$, $X^q_{RAF_{untrapped}}$ and X^q_{MAF} to the other temperatures where the reorientation times of the spin probe are collected by HF-EPR at 190 GHz, see Table 1. The results are plotted in Fig. 9

which may be read as a composition diagram of the non-crystalline part of $PDMS_q$. It is seen that, on increasing the temperature, the spin probe is increasingly located in MAF and less trapped in RAF.

3.5 Dynamic equilibrium of the spin probes in amorphous PDMS above T_g

Sec.3.4 discussed the partition of the spin probes in amorphous PDMS above T_g and identified three major contributions, namely the trapped and the untrapped spin probes in RAF, and the spin probes in MAF. The trapped spin probes have the smallest rotational mobility. The present section presents results concerning the dynamic equilibrium between the trapped spin probes and the ones with higher mobility. The results will be interpreted in a highly consistent way by a model based on a *reversible tertiary nucleation* scenario.

3.5.1 Dynamic Exchange Process

The trapped and the more mobile fractions of the spin probe in the non-crystalline region of PDMS above T_g have weights $X^q_{RAF_{trapped}}$ and $X^q_{MAF} + X^q_{RAF_{untrapped}}$, respectively. To quickly refer to the spatial regions where the two fractions are located and recognising that the mobility of the spin probes close to the crystallites is expectedly lower than that of the farther ones, we label as **C** and **F** the environments of the non-crystalline PDMS where the trapped and the more mobile fractions of the spin probe are located, respectively. A dynamic exchange process between the two fractions is anticipated. We tentatively model it as a "chemical reaction" thermodynamically equilibrated and consider the trapped and the more mobile fractions of the spin probe as the "reactant" and the "product", respectively. This scenario is sketched in the inset of Fig. 10. The related reaction equilibrium constant is:

$$K_{eq} = \frac{w_{PD}}{1 - w_{PD}} \tag{15}$$

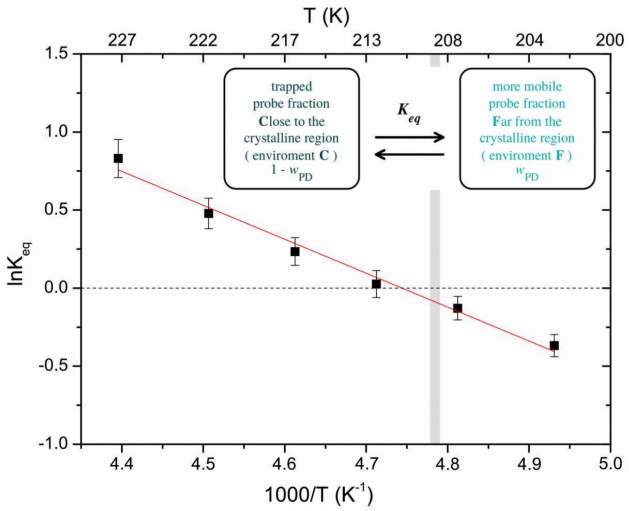

Figure 10: Van't Hoff plot of the equilibrium constant K_{eq}, Eq.15, between the trapped and the more mobile fractions of the spin probe in semicrystalline PDMS. Data concerning the quantity w_{PD} from Table 1. The straight red line is the best-fit with Eq.2 and $\Delta G_r^0 = \Delta H_r^0 - T\Delta S_r^0$. Detrapping involves positive standard enthalpy ($\Delta H_r^0 = 18 \pm 1$ kJ/mol) and entropy ($\Delta S_r^0 = 86 \pm 5$ J/K mol) of reaction. The gray region highlights the range of the onset of PDMS melting according to DSC ($\simeq 209$ K), see Sec.2.1. Notice that detrapping is favored, i.e. $\ln K_{eq}$ is positive and ΔG_r^0 is negative, if $T \gtrsim 209$ K. Inset: Equilibrium between the fractions of the spin probes located in the **C** and **F** environments of non-crystalline PDMS, being close to and far from the crystalline region, respectively. With reference to Fig.9, the **C** environment encloses the trapped fraction of the spin probes, whereas the other more mobile fractions are located in the **F** environment.

Eq.15 follows from Eq.13 and the relation $X^q_{MAF} + X^q_{RAF_{untrapped}} = w_{PD}$ drawn by Eq.9 and Eq.12. The quantity w_{PD} is listed in Table 1 for different temperatures. It must be stressed that Eq.15 relies *only* on the HF-EPR data.

Fig.10 presents the van't Hoff plot of the equilibrium constant K_{eq}, Eq.15. It is seen that the detrapping of the spin probe is favored, i.e. K_{eq} is larger than 1, if $T \gtrsim 209$ K, namely at temperatures higher than the onset of PDMS melting as detected by DSC which occurs at $\simeq 209$ K (see Sec.2.1).

Reminding Eq.2, one finds that the best-fit values of the standard Gibbs enthalpy and entropy of reaction drawn from Fig.10 are $\Delta H_r^0 = 18 \pm 1$ kJ and $\Delta S_r^0 = 86 \pm 5$ J/K per mole of spin probe. It should be observed that these parameters are dominated by the environments C and F and much less affected by the coupling of the spin probe with them.

In fact, assuming that the spin probes are very diluted, ΔG_r^0 may be written as:

$$\Delta G_r^0 = G_{pF} \; + \; G_F \; - \; G_{pC} \; - \; G_C \tag{16}$$

G_{pC} (G_{pF}) represents the molar free energy of interaction between the spin probe and the C (F) environment; G_C (G_F) represents the molar free energy of the C (F) environment hosting the spin probe. According to Eq.16 the standard enthalpy of reaction is $\Delta H_r^0 = H_{pF} + H_F - H_{pC} - H_C$. One notices that $\Delta H_r^0 = 18 \pm 1$ kJ/mol is much larger than the interaction energies between the spin probe and PDMS, see Table S.1 in the Supporting Information, so that it is safe to neglect $H_{pF} - H_{pC}$ and interpret ΔH_r^0 as

$$\Delta H_r^0 \simeq H_F - H_C \tag{17}$$

A similar conclusion is also reached for the standard entropy of reaction $\Delta S_r^0 = S_{pF} + S_F - S_{pC} - S_C$. In fact, one reminds that the spin probe the spin probe is quite stiff and nearly spherical, so that the (orientational) entropy change $S_{pF} - S_{pC}$ is negligible with respect to the difference $S_F - S_C$, namely

$$\Delta S_r^0 \simeq S_F - S_C \tag{18}$$

3.5.2 Reversible Tertiary Nucleation Scenario

Picturing the C and F environments as crystalline-like and liquid-like, respectively, provides a consistent interpretation of ΔH_r^0 and ΔS_r^0. To show that, we explore the proportionality betweeen the van't Hoff parameters ΔH_r^0 and ΔS_r^0 with the enthalpy and entropy of fusion per repeating PDMS unit, ΔH_m and ΔS_m, respectively:

$$\Delta H_r^0 \;\; = \;\; z_H \, \Delta H_m \tag{19}$$

$$\Delta S_r^0 \;\; = \;\; z_S \, \Delta S_m \tag{20}$$

where z_H and z_S are suitable constants depending on the microscopic features of the exchange process. We take $\Delta H_m = 4.619$ kJ/mol and $\Delta S_m = 19.6$ J/ K mol as listed in Ref.[71] . These values are in good agreement with a recent NMR study ($\Delta H'_m = 4.54$ kJ/mol[99]) and alternative sources ($\Delta S'_m = 19.1$ J/ K mol[100]). One finds $z_H = 3.9$ from Eq.19 and $z_S = 4.4$ from Eq. 20, i.e. the structural change of the surroundings of the spin probe from the trapped to the more mobile state is equivalent to the one of reversible "melting" of about $z \simeq 4$ PDMS monomers.

In order to rationalize the above findings, in particular the small difference between z_H and z_S, we picture the equilibrium sketched in the inset of Fig. 10 as due to a local process leading to freezing and subsequent melting of a region of z monomers - each with volume v_m - embedding one the spin probe molecule onto the surface of a crystallite. The process is an instance of secondary or tertiary nucleation with subsequent melting. We write the melting free energy change ΔG of the region as:[2]

$$\Delta G = \mathcal{N}_a[z\, v_m \Delta g_F - n v_m^{2/3}\gamma] \tag{21}$$

where $\Delta g_F = (\Delta H_m - T\Delta S_m)/(v_m \mathcal{N}_a)$, and $\mathcal{N}_a$, γ and $n v_m^{2/3}$ are the Avogadro number, the surface tension and the surface lost by the crystallite when the volume $z\, v_m$ melts, respectively. Comparing Eq.21 with $\Delta G_r^0 = \Delta H_r^0 - T\Delta S_r^0$ (ΔH_r^0 and ΔS_r^0 from Eq. 19 and Eq. 20 respectively) leads to:

$$z_H = z_S - \frac{v_m^{2/3}\gamma\mathcal{N}_a}{\Delta H_m}\, n \tag{22}$$

$$z_S = z \tag{23}$$

Eq.22 accounts for the finding $z_H < z_S$. To provide physical insight into the difference between z_H and z_S, we take $v_m = 0.138$ nm^3,[68] $\gamma = 22$ mJ/ m^2 [101] and find $v_m^{2/3}\gamma\mathcal{N}_a/\Delta H_m = 0.77$. From the experiment one has $z_S - z_H \sim 0.5$, yielding $n \sim 1$ for the lost surfaces. The result strongly suggests that the equilibrium process does not involve either primary (

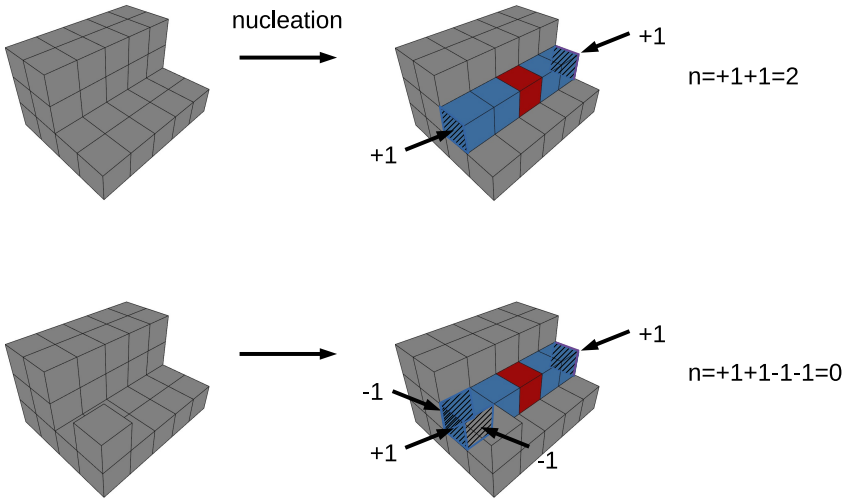

Figure 11: Schematic examples of tertiary nucleation of $z = 4$ PDMS monomers (light blue) surrounding one spin probe (red) at the intersections of pre-existent crystalline surfaces (gray). The drawing takes into account that the the spin probe size $V^{1/3} = 0.58$ nm is comparable to the monomer size $v_m^{1/3} = 0.51$ nm and the Kuhn length $\ell_K = 0.50$ nm.[68] Following the nucleation some crystalline faces appear (light-blue, hatched, marked as "+1") and other disappear (grey, hatched, marked as "-1"). The number of faces *gained* when nucleation occurs is denoted by n. The two sketches refer to nucleation yielding to the gain of two (top) and no (bottom) crystalline area units $v_m^{2/3}$. For clarity reasons, the pre-existing crystalline faces just shifted to a new position by nucleation are ignored since their overall contribution to n vanishes. Note that, in melting, which is the inverse process of nucleation, n represents the number of *lost* faces.

$n \sim 6z^{2/3} \sim 15$ with $z = 4$) or secondary ($n \sim 4z^{1/2} \sim 8$ with $z = 4$) nucleation[2] but rather tertiary ($n \lesssim 2$) nucleation which occurs at the intersection of crystalline surfaces. Some schematic examples are sketched in Fig.11. The above conclusion points to poor smoothness of the crystal-amorphous interface at a molecular level, as also suggested by similar findings in polyethylene.[9]

4 CONCLUSIONS

The reorientation of the spin probe spin probe in semicrystalline quench cooled PDMS has been investigated by means of HF-EPR spectroscopy at two different Larmor frequencies (190 and 285 GHz). The spin probe is confined outside the crystallites with homogeneous

distribution across all the amorphous fraction. Accurate numerical simulations evidence a distribution of reorientation times $\rho(\tau)$ above 200 K. The distribution exhibits a bimodal structure with: i) a narrow component corresponding to spin probes with extremely low rotational mobility trapped in a *glassy* RAF, located close to crystal and persisting up to T_m, and ii) a broad power-law component corresponding to spin probes with fast and intermediate rotational mobility, ascribed to spin probes located in MAF and in a "soft" RAF. Above the PDMS melting, occurring at about 230 K, the distribution narrows considerably.

The spin probe undergoes an exchange process between the trapped and the more mobile fractions which is accounted for by an equilibrium reversible process with standard Gibbs free energy of reaction $\Delta G_r^0 \simeq 4\,(\Delta H_m - T\Delta S_m)$, where ΔS_m is the equilibrium melting entropy per PDMS monomer mole following the absorption of the heat ΔH_m. We rule out that the exchange involves the migration of the *probe* between a crystalline-like and a liquid-like environment, but rather the exchange establishes through the interconversion of the *polymer* between the two different environments. The process is interpreted as signature of a reversible tertiary nucleation process. It becomes thermodynamically favored, i.e. ΔG_r^0 is negative, if $T \gtrsim 209$ K, namely at temperatures higher than the onset of PDMS melting as detected by DSC. Our finding suggests surface roughness of the crystal-amorphous interface at a molecular level as observed in polyethylene.[9] We point out that, even if we do not provide direct evidence of the above mentioned equilibrium, hypothesising this process offers a highly consistent interpretation of the HF-EPR results.

Acknowledgement

Helpful discussions with Monica Bertoldo, Giacomo Prampolini and Maria Cristina Righetti are gratefully acknowledged.

Supporting Information

Analysis of the coupling of the spin probe with PDMS host; outline of the rotational models

adopted in the numerical simulation of the HF-EPR Spectra

References

(1) Strobl, G. R. *The Physics of Polymers, III Ed.*; Springer: Berlin, 2007.

(2) Gedde, U. W. *Polymer Physics*; Chapman and Hall: London, 1995.

(3) Mandelkern, L. *The crystalline state*; in Physical Properties of Polymers, III Ed.; Cambridge University Press, Cambridge UK, 2004; pp 209–315.

(4) Wunderlich, B. Reversible crystallization and the rigid–amorphous phase in semicrystalline macromolecules. *Prog. Polym. Sci.* **2003**, *28*, 383–450.

(5) Strobl, G. Crystallization and melting of bulk polymers: New observations, conclusions and a thermodynamic scheme. *Prog. Polym. Sci.* **2006**, *31*, 398–442.

(6) Schick, C. Differential scanning calorimetry (DSC) of semicrystalline polymers. *Anal. Bioanal. Chem.* **2009**, *395*, 1589–1611.

(7) Righetti, M. C.; Laus, M.; Di Lorenzo, M. L. Temperature dependence of the rigid amorphous fraction in poly(ethylene terephthalate). *European Polymer Journal* **2014**, *58*, 60–68.

(8) Menczel, J. D. The rigid amorphous fraction in semicrystalline macromolecules. *Journal of Thermal Analysis and Calorimetry* **2011**, *106*, 7–24.

(9) Savage, R. C.; Mullin, N.; Hobbs, J. K. Molecular Conformation at the Crystal–Amorphous Interface in Polyethylene. *Macromolecules* **2015**, *48*, 6160–6165.

(10) Xu, H.; Cebe, P. Heat Capacity Study of Isotactic Polystyrene: Dual Reversible Crystal Melting and Relaxation of Rigid Amorphous Fraction. *Macromolecules* **2004**, *37*, 2797–2806.

(11) Loufakis, K.; Wunderlich, B. Thermal Analysis of the Conformational Disorder

in Semicrystalline Poly(viny1idene fluoride) and Poly(trifluoroethy1ene). *Macromolecules* **1987**, *20*, 2474–2478.

(12) Adachi, H.; Adachi, K.; Ishida, Y.; Kotaka, T. Dielectric Relaxation of Polydimethylsiloxane. *J. Polym. Sci. Pt. B-Polym. Phys.* **1979**, *17*, 851–857.

(13) Kirst, K. U.; Kremer, F.; Litvinov, V. M. Broad-Band Dielectric Spectroscopy on the Molecular Dynamics of Bulk and Adsorbed Poly(dimethylsi1oxane). *Macromolecules* **1993**, *26*, 975–980.

(14) Lorthioir, C.; Alegría, A.; Colmenero, J.; Deloche, B. Heterogeneity of the Segmental Dynamics of Poly(dimethylsiloxane) in a Diblock Lamellar Mesophase: Dielectric Relaxation Investigations. *Macromolecules* **2004**, *37*, 7808–7817.

(15) Lund, R.; Alegría, A.; Goitandí, L.; Colmenero, J.; González, M. A.; Lindner, P. Dynamical and Structural Aspects of the Cold Crystallization of Poly(dimethylsiloxane) (PDMS). *Macromolecules* **2008**, *41*, 1364–1376.

(16) Massa, C. A.; Pizzanelli, S.; Bercu, V.; Pardi, L.; Leporini, D. Constrained and Heterogeneous Dynamics in the Mobile and the Rigid Amorphous Fractions of Poly(dimethylsiloxane): A Multifrequency High-Field Electron Paramagnetic Resonance Study. *Macromolecules* **2014**, *47*, 6748–6756.

(17) Massa, C. A.; Pizzanelli, S.; Bercu, V.; Pardi, L.; Bertoldo, M.; Leporini, D. A High-Field EPR Study of the Accelerated Dynamics of the Amorphous Fraction of Semicrystalline Poly(dimethylsiloxane) at the Melting Point. *Appl. Magn. Reson.* **2014**, *45*, 693–706.

(18) Saiter, A.; Delpouve, N.; Dargent, E.; Oberhauser, W.; Conzatti, L.; Cicogna, F.; Passaglia, E. Probing the chain segment mobility at the interface of semi-crystalline polylactide/clay nanocomposites. *European Polymer Journal* **2016**, *78*, 274–289.

(19) Ma, Q.; Georgiev, G.; Cebe, P. Constraints in semicrystalline polymers: using quasi-isothermal analysis to investigate the mechanisms of formation and loss of the rigid amorphous fraction. *Polymer* **2011**, *52*, 4562–4570.

(20) Esposito, A.; Delpouve, N.; Causin, V.; Dhotel, A.; Delbreilh, L.; Dargent, E. From a Three-Phase Model to a Continuous Description of Molecular Mobility in Semicrystalline Poly(hydroxybutyrate-co-hydroxyvalerate). *Macromolecules* **2016**, *49*, 4850–4861.

(21) Klonos, P.; Kulyk, K.; Borysenko, M. V.; Gun'ko, V. M.; Kyritsis, A.; Pissis, P. Effects of Molecular Weight below the Entanglement Threshold on Interfacial Nanoparticles/Polymer Dynamics. *Macromolecules* **2016**, *49*, 9457–9473.

(22) Klonos, P.; Dapei, G.; Sulym, I. Y.; Zidropoulos, S.; Sternik, D.; Deryło-Marczewska, A.; Borysenko, M. V.; Gun'ko, V. M.; Kyritsis, A.; Pissis, P. Morphology and molecular dynamics investigation of PDMS adsorbed on titania nanoparticles: Effects of polymer molecular weight. *European Polymer Journal* **2016**, *74*, 64–80.

(23) Gin, P.; Jiang, N.; Liang, C.; Taniguchi, T.; Akgun, B.; Satija, S. K.; Endoh, M. K.; Koga, T. Revealed Architectures of Adsorbed Polymer Chains at Solid-Polymer Melt Interfaces. *Phys. Rev. Lett.* **2012**, *109*, 265501.

(24) Rotella, C.; Napolitano, S.; Vandendriessche, S.; Valev, V. K.; Verbiest, T.; Larkowska, M.; Kucharski, S.; Wübbenhorst, M. Adsorption Kinetics of Ultrathin Polymer Films in the Melt Probed by Dielectric Spectroscopy and Second-Harmonic Generation. *Langmuir* **2011**, *27*, 13533–13538.

(25) Wunderlich, B. *Thermal Analysis of Polymeric Materials*; Springer, Berlin, 2005.

(26) Albrecht, T.; Armbruster, S.; Keller, S.; Strobl, G. Dynamics of Surface Crystallization and Melting in Polyethylene and Poly(ethylene oxide) Studied by Temperature-Modulated DSC and Heat Wave Spectroscopy. *Macromolecules* **2001**, *34*, 8456–8467.

(27) Wurm, A.; Merzlyakov, M.; Schick, C. Reversible Melting During Crystallization of Polymers Studied by Temperature Modulated Techniques (TMDSC, TMDMA). *J. Therm. Anal. Calorim.* **2000**, *60*, 807–820.

(28) Okazaki, I.; Wunderlich, B. Reversible Melting in Polymer Crystals Detected by Temperature-Modulated Differential Scanning Calorimetry. *Macromolecules* **1997**, *30*, 1758–1764.

(29) Righetti, M. C.; Di Lorenzo, M. L.; Angiuli, M.; Tombari, E. Structural Reorganization in Poly(butylene terephthalate) during Fusion. *Macromolecules* **2004**, *37*, 9027–9033.

(30) Hu, W.; Albrecht, T.; Strobl, G. Reversible Surface Melting of PE and PEO Crystallites Indicated by TMDSC. *Macromolecules* **1999**, *32*, 7548–7554.

(31) Barra, F.; Esposito, M. Dissipation in small systems: Landau-Zener approach. *Phys. Rev. E* **2016**, *93*, 062118.

(32) de Groot, S. R.; Mazur, P. *Non-equilibrium Thermodynamics*; Dover Publications, New York, 1984.

(33) Crooks, G. E. On thermodynamic and microscopic reversibility. *J. Stat. Mech.* **2011**, P07008.

(34) Tolman, R. C. *The Principles of Statistical Mechanics*; Oxford University Press, London, 1938.

(35) Gaveau, B.; Moreau, M.; Schulman, L. S. Generalized Clausius relation and power dissipation in nonequilibrium stochastic systems. *Phys. Rev. E* **2009**, *79*, 010102(R).

(36) Barbieri, A.; Gorini, G.; Leporini, D. Role of the density in the crossover region of o-terphenyl and poly(vinyl acetate). *Phys. Rev. E* **2004**, *69*, 061509.

(37) Roos, M.; Schäler, K.; Seidlitz, A.; Thurn-Albrecht, T.; Saalwächter, K. NMR study of interphase structure in layered polymer morphologies with mobility contrast: disorder

and confinement effects vs. dynamic heterogeneities. *Colloid Polym. Sci.* **2014**, *292*, 1825–1839.

(38) Schmidt-Rohr, K.; Spiess, H. W. *Multidimensional Solid-State NMR and Polymers*; Academic Press, London, 1994.

(39) Alegria, A.; Colmenero, J. Dielectric relaxation of polymers: segmental dynamics under structural constraints. *Soft Matter* **2016**, *12*, 7709–7725.

(40) Dorio, M. M.; Chien, J. C. W. A Study of Molecular Motion in Polymeric Solids by Electron-ElectronDouble Resonance. *Macromolecules* **1975**, *8*, 734–739.

(41) Kutsumizu, S.; Goto, M.; Yano, S. Electron Spin Resonance Studies on Sodium-Neutralized Ethylene Ionomers: Microphase-Separated Structure and Thermal Behaviors. *Macromolecules* **2004**, *37*, 4821–4829.

(42) Massa, C. A.; Pizzanelli, S.; Bercu, V.; Pardi, L.; Leporini, D. *Applied Magnetic Resonance*, 2017, DOI: 10.1007/s00723-017-0903-z.

(43) Berliner, L. J., Reuben, J., Eds. *Biological Magnetic Resonance*; Plenum, New York, 1989.

(44) Ross, R. Dipolar broadening of EPR spectra due to solute segregation in frozen aqueous solution. *J.Chem. Phys* **1965**, *42*, 3919–3922.

(45) Leigh Jr., J. S.; Reed, G. H. Electron paramagnetic resonance studies in frozen aqueous solutions. Elimination of freezing artifacts. *J. Phys. Chem.* **1971**, *75*, 1202–1204.

(46) Ahn, M.-K. Electron spin relaxation of di-tertiary-butyl nitroxide in supercooled water. *J. Chem. Phys.* **1976**, *64*, 134–138.

(47) Banerjee, D.; S.N.Bhat,; S.V.Bhat,; Leporini, D. ESR evidence for 2 coexisting liquid phases in deeply supercooled bulk water. *Proc. Natl. Acad. Sci. USA* **2009**, *106*, 11448–11453.

(48) Banerjee, D.; S.N.Bhat,; S.V.Bhat,; Leporini, D. Molecular Probe Dynamics Reveals Suppression of Ice- Like Regions in Strongly Confined Supercooled Water. *PLOS ONE* **2012**, *7*, e44382.

(49) Banerjee, D.; Bhat, S. V.; D.Leporini, Electron Spin Resonance Studies of Supercooled Water. *Adv. Chem. Phys.* **2013**, *152*, 1–28.

(50) Boyer, R. F. Mechanical motions in amorphous and semi-crystalline polymers. *Polymer* **1976**, *17*, 996–1008.

(51) Törmälä, P. Spin Label and Probe Studies of Polymeric Solids and Melts. *Journal of Macromolecular Science, Part C* **1979**, *17*, 297–357.

(52) Rånby, B.; J.Rabek, *ESR Spettroscopy in Polymer Research*; Springer, Berlin, 1977.

(53) Faetti, M.; Giordano, M.; Leporini, D.; Pardi, L. Scaling Analysis and Distribution of the Rotational Correlation Times of a Tracer in Rubbery and Glassy Poly(vinyl acetate): An Electron Spin Resonance Investigation. *Macromolecules* **1999**, *32*, 1876–1882.

(54) Leporini, D.; Schädler, V.; Wiesner, U.; Spiess, H. W.; Jeschke, G. Electron spin relaxation due to small-angle motion: Theory for the canonical orientations and application to hierarchic cage dynamics in ionomers. *J. Chem. Phys.* **2003**, *119*, 11829–11846.

(55) Bercu, V.; Martinelli, M.; Massa, C. A.; Pardi, L. A.; Leporini, D. A study of the deep structure of the energy landscape of glassy polystyrene: the exponential distribution of the energy-barriers revealed by high-field Electron Spin Resonance spectroscopy. *Journal of Physics: Condensed Matter* **2004**, *16*, L479–L488.

(56) Bercu, V.; Martinelli, M.; Pardi, L.; Massa, C. A.; Leporini, D. Dynamical Line-Shifts in High-Field Electron Spin Resonance: Applications to Polymer Physics. *Zeitschrift für Physikalische Chemie* **2012**, *226*, 1379–1394.

(57) Bercu, V.; Martinelli, M.; Massa, C. A.; Pardi, L. A.; Leporini, D. Signatures of the fast dynamics in glassy polystyrene: First evidence by high-field Electron Paramagnetic Resonance of molecular guests. *J. Chem. Phys.* **2005**, *123*, 174906.

(58) McCrum, N. G.; Read, B. E.; Williams, G. *Anelastic and Dielectric Effects in Polymeric Solids*; Dover Publications: New York, 1991.

(59) Ngai, K. L. *Relaxation and Diffusion in Complex Systems*; Springer, Berlin, 2011.

(60) Ngai, K. L.; Roland, C. M. Intermolecular Cooperativity and the Temperature Dependence of Segmental Relaxation in Semicrystalline Polymers. *Macromolecules* **1993**, *26*, 2688–2690.

(61) Larini, L.; Barbieri, A.; Prevosto, D.; Rolla, P. A.; Leporini, D. Equilibrated polyethylene single-molecule crystals: molecular-dynamics simulations and analytic model of the global minimum of the free-energy landscape. *J. Phys.: Condens. Matter* **2005**, *17*, L199–L208.

(62) Cocca, M.; Lorenzo, M. L. D.; Malinconico, M.; Frezza, V. Influence of crystal polymorphism on mechanical and barrier properties of poly(L-lactic acid). *Eur. Pol. J.* **2011**, *47*, 1073–1080.

(63) Drieskens, M.; Peeters, R.; Mullens, J.; Franco, D.; Lemstra, P. J.; Hristova-Bogaerds, D. G. Structure versus properties relationship of poly(lactic acid). I. Effect of crystallinity on barrier properties. *J.Polym.Sci Part B: Polym. Phys.* **2009**, *47*, 2247–2258.

(64) George, S. C.; Thomas, S. Transport phenomena through polymeric systems. *Prog. Polym. Sci.* **2001**, *26*, 985–1017.

(65) Klopffer, M.; Flaconnèche, B. Transport Properties of Gases in Polymers: Bibliographic Review. *Oil & Gas Science and Technology* **2001**, *56*, 223–244.

(66) Klonos, P.; Kyritsis, A.; Pissis, P. Effects of surface modification and thermal annealing on the interfacial dynamics in core–shell nanocomposites based on silica and adsorbed PDMS. *European Polymer Journal* **2015**, *70*, 342–359.

(67) Soegiarto, A. C.; Yan, W.; Kentab, A. D.; Ward, M. D. Regulating low-dimensional magnetic behavior of organic radicals in crystalline hydrogen-bonded host frameworks. *J. Mat. Chem.* **2011**, *21*, 2204–2219.

(68) Eitouni, H. B.; Balsara, N. P. In *Physical Properties of Polymers Handbook, II Ed.*; Mark, J. E., Ed.; Springer, Berlin, 2007; pp 339–356.

(69) Saalmueller, J. W.; Long, H. W.; Volkmer, T.; Wiesner, U.; Maresch, G. G.; Spiess, H. W. Characterization of the motion of spin probes and spin labels in amorphous polymers with two-dimensional field-step ELDOR. *J. Polym. Sci. Pt. B-Polym. Phys.* **1996**, *34*, 1093–1104.

(70) Soutzidou, M.; Panas, A.; Viras, K. Differential scanning calorimetry (DSC) and Raman spectroscopy study of poly(dimethylsiloxane). *J. Polym. Sci. Part B Polym. Phys.* **1998**, *36*, 2805–2810.

(71) Mandelkern, L.; Alamo, R. G. In *Physical Properties of Polymers Handbook, II Ed.*; Mark, J. E., Ed.; Springer, Berlin, 2007; pp 165–186.

(72) Brunel, L. C.; Caneschi, A.; Dei, A.; Friselli, D.; Gatteschi, D.; Hassan, A. K.; Lenci, L.; Martinelli, M.; Massa, C. A.; Pardi, L. A.; Popescu, F.; Ricci, I.; Sorace, L. How and why the characterization of magnetic materials can give directions in the methodological development in high field–high frequency EPR. *Research on Chemical Intermediates* **2002**, *28*, 215–229.

(73) Giordano, M.; Grigolini, P.; Leporini, D.; Marin, P. Fast-computational approach to the evaluation of slow-motion EPR spectra in terms of a generalized Langevin equation. *Phys. Rev. A* **1983**, *28*, 2474–2481.

(74) Stoll, S.; Schweiger, A. EasySpin, a comprehensive software package for spectral simulation and analysis in EPR. *Journal of Magnetic Resonance* **2006**, *178*, 42–55.

(75) Budil, D. E.; Lee, S.; Saxena, S.; Freed, J. H. Nonlinear-Least-Squares Analysis of Slow-Motion EPR Spectra in One and Two Dimensions Using a Modified Levenberg–Marquardt Algorithm. *Journal of Magnetic Resonance, Series A* **1996**, *120*, 155–189.

(76) Alessi, L.; Andreozzi, L.; Faetti, M.; Leporini, D. Anisotropic jump model of the rotational dynamics in glasses. *J.Chem.Phys.* **2001**, *114*, 3631–3639.

(77) Cheng, S. Z. D.; Cao, M. Y.; Wunderlich, B. Glass transition and melting behavior of poly(oxy-1,4-phenyleneoxy-1,4-phenylenecarbonyl-1,4-phenylene) (PEEK). *Macromolecules* **1986**, *19*, 1868–1876.

(78) Cheng, S. Z. D.; Wu, Z. Q.; Wunderlich, B. Glass transition and melting behavior of poly(thio-1,4-phenylene). *Macromolecules* **1987**, *20*, 2802–2810.

(79) Cheng, S. Z. D.; Pan, R.; Wunderlich, B. Thermal analysis of poly(butylene terephthalate) for heat capacity, rigid-amorphous content, and transition behavior. *Die Makromolekulare Chemie* **1988**, *189*, 2443–2458.

(80) Meyer, H. In *Polymer Crystallization: Obervations, Concepts and Interpretations*; Reiter, G., Sommer, J.-U., Eds.; Springer, Berlin, 2008; Chapter 10.

(81) Wang, X.; Ouyang, J. Phase-Field Simulation of Polymer Crystallization during Cooling Stage. *International Journal of Chemical Engineering and Applications* **2015**, *6*, 28–31.

(82) St-Onge, H. A Study of Morphology in Polyethylene Filled with 3-Percent Carbon. *IEEE Transactions on Electrical Insulation* **1980**, *EI-15*, 359–361.

(83) Hong, P.-D.; Chuang, W.-T.; Yeh, W.-J.; Lin, T.-L. Effect of rigid amorphous phase

on glass transition behavior of poly(trimethylene terephthalate). *Polymer* **2002**, *43*, 6879–6886.

(84) Lin, J.; Shenogin, S.; Nazarenko, S. Oxygen solubility and specific volume of rigid amorphous fraction in semicrystalline poly(ethylene terephthalate). *Polymer* **2002**, *43*, 4733–4743.

(85) Huo, P.; Cebe, P. Effects of thermal history on the rigid amorphous phase in poly(phenylene sulfide). *Colloid and Polymer Science* **1992**, *270*, 840–852.

(86) Fragiadakis, D.; Pissis, P.; Bokobza, L. Glass transition and molecular dynamics in poly(dimethylsiloxane)/silica nanocomposites. *Polymer* **2005**, *46*, 6001–6008.

(87) Fragiadakis, D.; Pissis, P.; Bokobza, L. Modified chain dynamics in poly(dimethylsiloxane)/silica nanocomposites. *J. Non-Cryst. Solids* **2006**, *352*, 4969–4972.

(88) Schroeder, M. J.; Roland, C. M. Segmental Relaxation in End-Linked Poly(dimethylsiloxane) Networks. *Macromolecules* **2002**, *35*, 2676–2681.

(89) Cherdhirankorn, T.; Harmandaris, V.; Juhari, A.; Voudouris, P.; Fytas, G.; Kremer, K.; Koynov, K. Fluorescence Correlation Spectroscopy Study of Molecular Probe Diffusion in Polymer Melts. *Macromolecules* **2009**, *42*, 4858–4866.

(90) Hwang, J. S.; Mason, R. P.; Hwang, L. P.; Freed, J. H. Electron spin resonance studies of anisotropic rotational reorientation and slow tumbling in liquid and frozen media. III. Perdeuterated 2,2,6,6-tetramethyl-4-piperidone N-oxide and an analysis of fluctuating torques. *The Journal of Physical Chemistry* **1975**, *79*, 489–511.

(91) Andreozzi, L.; Di Schino, A.; Giordano, M.; Leporini, D. Evidence of a fractional Debye-Stokes-Einstein law in supercooled oterphenyl. *Europhys. Lett.* **1997**, *38*, 669–674.

(92) Khambatta, F. B.; Warner, F.; Russell, T.; Stein, R. S. Small-angle x-ray and light scattering studies of the morphology of blends of poly(ϵ-caprolactone) with poly(vinyl chloride). *Journal of Polymer Science: Polymer Physics Edition* **1976**, *14*, 1391–1424.

(93) Mandelkern, L.; Alamo, R. G.; Kennedy, M. A. The interphase thickness of linear polyethylene. *Macromolecules* **1990**, *23*, 4721–4723.

(94) Lisowski, M. S.; Liu, Q.; Cho, J.; Runt, J.; Yeh, F.; Hsiao, B. S. Crystallization Behavior of Poly(ethylene oxide) and Its Blends Using Time-Resolved Wide- and Small-Angle X-ray Scattering. *Macromolecules* **2000**, *33*, 4842–4849.

(95) Grapengeter, H. H.; Alefeld, B.; Kosfeld, R. An investigation of micro-brownian motions in polydimethylsiloxane by complementary incoherent-neutron-scattering and nuclear-magnetic-resonance experiments below room temperature. *Colloid Polym. Sci.* **1987**, *265*, 226–233.

(96) Arrighi, V.; Gagliardi, S.; Zhang, C.; Ganazzoli, F.; Higgins, J. S.; Ocone, R.; Telling, M. T. F. A Unified Picture of the Local Dynamics of Poly(dimethylsiloxane) across the Melting Point. *Macromolecules* **2003**, *36*, 8738–8748.

(97) Ferry, J. D. *Viscoelastic properties of polymers,* III Ed.; Wiley, New York, 1980.

(98) Sawyer, L. C.; Grubb, D. T.; Meyers, G. F. *Polymer Microscopy, III Ed.*; Springer, Berlin, 2008.

(99) Maus, A.; Saalwächter, K. Crystallization Kinetics of Poly(dimethylsiloxane) Molecular-Weight Blends—Correlation with Local Chain Order in the Melt? *Macromolecular Chemistry and Physics* **2007**, *208*, 2066–2075.

(100) Privalko, V. P. Excess Entropies and Related Quantities in Glass-Forming Liquids. *J. Phys. Chem.* **1980**, *84*, 3307–3312.

(101) Chaudhury, M. K. Interfacial interaction between low-energy surfaces. *Materials Science and Engineering* **1996**, *R16*, 97–159.

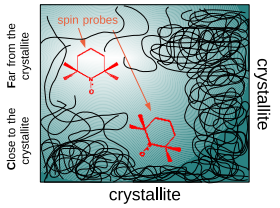

for Table of Contents use only

Local Reversible Melting in Semicrystalline Poly (dimethylsiloxane): a High-Field Electron Paramagnetic Resonance Study

Carlo Andrea Massa, Silvia Pizzanelli, Vasile Bercu, Luca Pardi, and Dino Leporini